Characterization of the near-surface gas-phase chemical environment in atmospheric-pressure plasma chemical vapor deposition of diamond

J.M. Larson, M.T. Swihart [1], S.L. Girshick *

Department of Mechanical Engineering, University of Minnesota, 111 Church St. SE, Minneapolis, MN 55455, USA

Abstract

A numerical model was developed and used to study the near-surface gas-phase chemistry during atmospheric-pressure radio-frequency (RF) plasma diamond chemical vapor deposition (CVD). Model predictions of the mole fractions of CH_4, C_2H_2, C_2H_4 and C_2H_6 agree well with gas chromatograph measurements of those species over a broad range of operating conditions. The numerical model includes a two-dimensional analysis of the sampling disturbance in the thin boundary layer above the substrate, accounts for chemistry in the gas chromatography sampling line, and utilizes a reaction mechanism that is significantly revised from a previously reported version. The model is used to predict the concentrations of H, CH_3, C_2H_2 and C at the diamond growth surface. It is suggested that methyl, acetylene and atomic carbon may all contribute significantly to film deposition during atmospheric-pressure RF plasma diamond CVD. The growth mechanism used in the model is shown to predict growth rates well at moderate substrate temperatures (~ 1100 to 1230 K) but less well for lower (~ 1000 K) and higher (~ 1300 K) temperatures. The near-surface gas-phase chemical environment in atmospheric-pressure RF plasma diamond CVD is compared with several other diamond CVD environments. Compared with these other methods the thermal plasma is predicted to produce substantially higher concentration ratios at the surface of both H/CH_3 and C_2H_2/CH_3. © 1999 Elsevier Science S.A. All rights reserved.

Keywords: Chemical vapor deposition; Diamond; Radio-frequency plasmas; Thermal plasmas

1. Introduction

Atmospheric-pressure plasmas are among the most promising methods for chemical vapor deposition (CVD) of diamond because of the high growth rates and the practical advantages of atmospheric-pressure operation. Although it is generally accepted that the gas-phase chemical composition at the diamond surface strongly affects diamond growth, few experimental and modeling studies have been reported that characterize this environment during atmospheric-pressure thermal plasma diamond CVD. For atmospheric-pressure inductively coupled radio-frequency (RF) thermal plasmas, measurements by Owano and coworkers of CH [1] and

C_2 [2] concentrations using degenerate four-wave mixing spectroscopy were compared with a numerical model [2]. It was found that CH measurements were in good agreement with the model, whereas the measured C_2 concentrations close to the substrate were two orders of magnitude above the model predictions [2]. Our own measurements of CH_4, C_2H_2, C_2H_4, C_2H_6, H_2 and Ar by gas chromatography (GC) [3] were compared with a preliminary numerical model [4]. The model predictions of the CH_4, C_2H_4 and C_2H_6 mole fractions at the growth surface were approximately one order of magnitude greater than the GC measurements, although agreement was improved by qualitatively accounting for sampling effects [4].

Two improvements have been made to that preliminary model. First, a detailed two-dimensional model was developed to characterize the disturbance caused by the sonic orifice used for gas sampling [5]. Second, the reaction mechanism used for modeling gas-phase finite-rate chemical kinetics in the boundary layer above

---

* Corresponding author. Tel.: +1-612-625-5315; fax: +1-612-624-5320.

E-mail address: slg@tc.umn.edu (S.L. Girshick).

[1] Present address: Department of Chemical Engineering, SUNY Buffalo, Buffalo, NY 14260-4200, USA.

Table 1
Operating conditions

Variable	Typical value
Pressure	1 atm
Power supply	2.9 MHz at plate power of 13 kW
Primary argon	40 slm
Probe $Ar/H_2/CH_4$	4 slm/4 slm/40–200 sccm
CH_4/H_2	1–6%
Substrate temperature	1000–1400 K

the growth substrate was revised from the version used previously [4]. Several reaction mechanisms have been presented for gas-phase chemistry in diamond CVD systems depending on the nature of the growth environment [6–10].[2] Although detailed numerical models for hot filament [7,9] and flame [11,12] diamond CVD systems have yielded good agreement with experimental measurements of several species [9,11–16], to our knowledge there has been no comparable validation of a numerical model applicable to thermal plasma diamond CVD systems.

In this paper we present a comparison of CH_4, C_2H_2, C_2H_4, and C_2H_6 mole fractions predicted by the revised model to previously reported GC measurements [3]. The numerical simulations and GC measurements are shown to agree over a broad range of substrate temperatures and input reactant compositions. The model is used to study the near-surface gas-phase chemical composition in our thermal plasma system, including the concentrations of free radical species that are difficult to measure. Comparisons are made with other diamond CVD environments.

2. Experimental

The numerical model simulates experiments described in detail elsewhere [3]. Briefly, the flow configuration is the 'central jet injection' geometry in which reactants are coaxially injected through a probe inserted directly into the coil region of an RF plasma [17,18]. A 2.9 MHz generator operating at 13 kW was used for the atmospheric-pressure induction plasma torch. The argon flowrate at the torch inlet was 40 slm, and the flowrates of argon and hydrogen introduced through the probe were each 4 slm. Methane was injected through the probe at 1 to 6% of the hydrogen flowrate. Operating conditions are summarized in Table 1. The temperature of the molybdenum substrate was controlled automatically by a previously described substrate cooling system [19].

---

[2] The mechanism of Miller and Melius [6], although not developed for flame diamond CVD, has been used in numerical models of these systems [11,12].

Gas was sampled through a 70 µm diameter sonic orifice located at the center of the substrate and delivered through a sampling line to a gas chromatograph for analysis. The sampling line was maintained at 20 Torr upstream of the gas chromatograph sampling loop, dropping to 6 Torr downstream of the sampling loop. Concentrations were measured using a thermal conductivity detector and a flame ionization detector connected in series. Calibrated measurements of Ar, H_2, CH_4, C_2H_2, C_2H_4, and C_2H_6 mole fractions were made as the substrate temperature and the input methane/hydrogen ratio were varied [3].

Two sampling effects must be considered when interpreting the GC data: the disturbance and finite spatial resolution caused by gas sampling through the sonic orifice, and the chemical reactions that occur in the sampling line from the substrate to the gas chromatograph. Suction by the sonic orifice causes a perturbation of the flow and temperature fields near the orifice compared with ideal stagnation-point flow conditions. The hot gas is accelerated from near zero velocity close to the substrate to sonic velocity in the orifice throat. Because there is no surface at the orifice itself the gas temperature at the orifice inlet is higher than the surrounding substrate temperature. Thus the character of the flow near the orifice changes from a one-dimensional stagnation-point flow to an axisymmetric two-dimensional flow. As a result the one-dimensional model used in our previously reported preliminary model is inaccurate in the region near the orifice [4]. Recently, we developed a fully two-dimensional model to simulate the flow near the orifice [5].

To characterize the sampling line chemistry we performed one-dimensional kinetic calculations similar to those described by Harris and Weiner [14]. This model is described and discussed below.

3. Numerical model

Fig. 1 shows our general approach to modeling the RF plasma diamond CVD system. Three sub-models — a plasma model, a boundary layer model, and a gas chromatograph sampling line model — were used to simulate the diamond deposition reactor and gas chromatograph sampling system. Together, the models predict the composition of the gas arriving at the diamond surface and at the gas chromatograph.

The axisymmetric plasma is modeled in two dimensions by solving the continuum fluid conservation equations coupled to the electromagnetic field equations for an argon–hydrogen gas mixture (hydrocarbons, which comprise less than 0.2% by volume of the total flow, are neglected) [10,17]. This calculation determines the flow field, temperature, and H, H_2 and Ar concentrations throughout the reactor, but does not resolve the thin
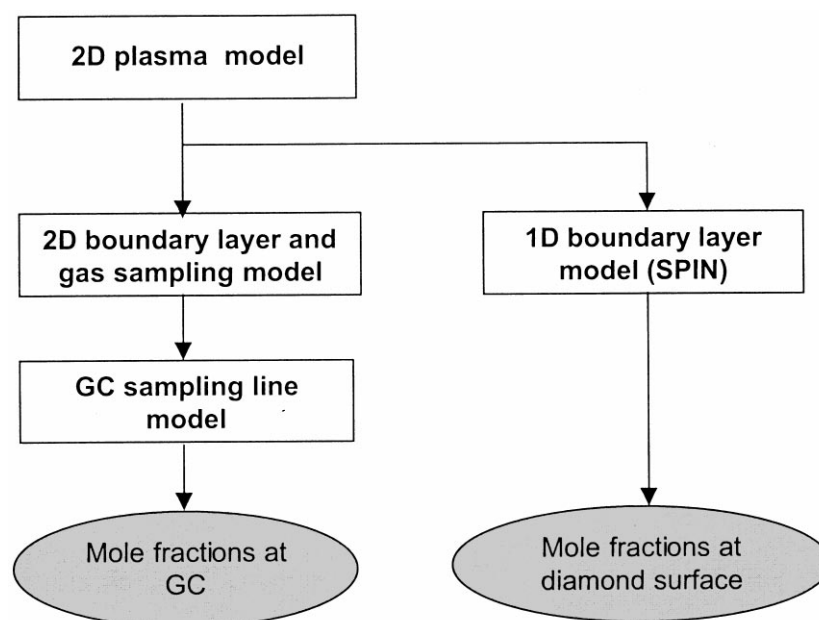
Fig. 1. Modeling of the RF plasma diamond CVD system.

reacting boundary layer above the substrate. For the flow conditions considered here the two-dimensional plasma model predicts the 4000 K isotherm to lie 2.0 mm above the substrate. We take this location to define the edge of the chemically reacting boundary layer. For these conditions the plasma model predicts an axial velocity of 9.7 m/s at the boundary layer edge.

A two-dimensional model is used to simulate the reacting boundary layer and the flow into the sampling orifice [5]. This model quantifies the disturbance due to the flow into the sampling orifice, and predicts the gas-phase concentrations and surface coverages. Detailed, finite-rate chemical kinetics are simulated both in the gas phase and at the surface. The surface mechanism is the growth-by-C_1-radicals mechanism of Yu and Girshick [18], which is an extended version of the growth-by-methyl mechanism of Harris [20]. The gas-phase mechanism is described in detail below. The temperature dependence of surface site free energies is calculated assuming constant specific heat and using reference free energies at 1200 K [18,21]. The simulations were performed using the computational fluid dynamics code CFD-ACE [22]. The transport coefficients for the 2-D boundary layer model were calculated from the kinetic theory expressions, as given in Refs. [23,24]. Thermal diffusion is important in this system and was included. Concentration- and temperature-dependent mixture-averaged diffusion coefficients were used to describe ordinary diffusion. A zero gradient boundary condition was applied at the radial outflow boundary for temperature, radial velocity, and all species concentrations. The imposed pressure profile was the profile that would be present in an ideal stagnation point flow. The computational domain extends axially from 2 mm above the substrate to about 2 mm down-stream of the sampling orifice and has a radius above the substrate of 2 mm.

The core of the gas-phase reaction mechanism utilizes hydrocarbon reactions found in the GRI mechanism for methane combustion [25]. Several reactions involving atomic carbon were added to the mechanism, because at 4000 K, 1 atm, and typical inlet methane concentrations for this system, around 90% of the carbon is in the form of atomic carbon. The complete mechanism and references for the rate parameters are given in Table 2. Because the peak temperature in these calculations is 4000 K, rate parameters for many of the reactions are extrapolated from measurements or calculations at lower temperatures. This adds substantial uncertainty to the reaction rates. However, many reactions in this system are near equilibrium over most of the reactor domain, particularly at positions where the temperature is highest and the rate parameters are the least certain. Reaction equilibria are determined by thermochemical parameters taken from the CHEMKIN thermodynamic database [37]. The parameters are valid up to 5000 K for all compounds in the mechanism except for C_2H_6, CH_2, $CH_2(S)$ and C_2H, for which the upper limit is 4000 K. As a result, reaction equilibria are accurately determined up to 4000 K. By reviewing the most recent kinetics literature, high temperature rate parameters were chosen when available. Finally, an important addition to this mechanism compared with the mechanism used in the preliminary model is that we account for the pressure dependence of reaction 18 in Table 2, $CH_3 + H(+M) \Leftrightarrow CH_4(+M)$. This effect had

Table 2
Gas-phase reaction mechanism. Forward rate constants are expressed in the form $k_f = AT^\beta exp(-E/RT)$

Reaction		A (cm³ mol s)	β	E_a (cal/mol)	Reference
Hydrogen recombination					
1.[a]	$2H + M \Leftrightarrow H_2 + M$	1.00×10^{18}	-1	0	[25]
	Eenhanced third-body efficiencies: $H_2 = 0.0$, $Ar = 0.63$				
2.	$2H + H_2 \Leftrightarrow 2H_2$	9.00×10^{16}	-0.6	0	[25]
H transfer from H$_2$					
3.[a]	$CH + H \Leftrightarrow C + H_2$	1.10×10^{14}	0	0	[26]
4.[a]	$CH + H_2 \Leftrightarrow CH_2 + H$	2.20×10^{10}	1.022	2504	[27]
5.	$CH_2 + H_2 \Leftrightarrow CH_3 + H$	5.00×10^5	2	7230	[25]
6.[a]	$CH_3 + H_2 \Leftrightarrow CH_4 + H$	6.90×10^3	2.74	9420	[28]
7.[a]	$C_2 + H_2 \Leftrightarrow C_2H + H$	6.60×10^{13}	0	7950	[29]
8.[a]	$C_2H + H_2 \Leftrightarrow C_2H_2 + H$	7.90×10^5	2.39	346	[30]
9.[a,b]	$C_2H_3 + H \Leftrightarrow C_2H_2 + H_2$	3.00×10^{13}	0	0	
10.[a]	$C_2H_3 + H_2 \Leftrightarrow C_2H_4 + H$	9.45×10^3	2.56	1270	[28]
11.	$C_2H_5 + H \Leftrightarrow C_2H_4 + H_2$	2.00×10^{12}	0	0	[25]
12.[a]	$C_2H_6 + H \Leftrightarrow C_2H_5 + H_2$	1.15×10^8	1.9	7530	[25]
Dissociations/recombinations with H and H$_2$					
13.	$CH + M \Leftrightarrow C + H + M$	1.90×10^{14}	0	66 960	[31]
14.	$CH_2 + M \Leftrightarrow CH + H + M$	5.60×10^{15}	0	89 630	[32]
15.[a]	$CH_2 + M \Leftrightarrow C + H_2 + M$	1.50×10^{14}	0	63 800	[32]
16.[a]	$CH_3 + M \Leftrightarrow CH_2 + H + M$	2.00×10^{16}	0	90 600	[31]
17.[a]	$CH_3 + M \Leftrightarrow CH + H_2 + M$	5.00×10^{15}	0	85 000	[31]
18.[a,c]	$CH_3 + H(+M) \Leftrightarrow CH_4(+M)$				[25]
	High-pressure limit:	1.27×10^{16}	-0.63	383	
	Low-pressure limit:	2.48×10^{33}	-4.76	2440	
	Troe parameters: $a = 0.783$, $T^* = 2941.0$, $T^{**} = 6964.0$, $T^{***} = 74.0$				
	Enhanced third-body efficiencies: $H_2 = 2.0$, $Ar = 0.70$				
19.[a]	$C_2H + M \Leftrightarrow C_2 + H + M$	1.74×10^{35}	-5.16	114 000	[29]
20.[a]	$C_2H_2 + M \Leftrightarrow C_2H + H + M$	6.96×10^{39}	-6.06	133 400	[29]
21.[a]	$C_2H_2 + H(+M) \Leftrightarrow C_2H_3(+M)$				[25]
	High-pressure limit:	5.60×10^{12}	0	2400	
	Low-pressure limit:	3.80×10^{40}	-7.27	7220	
	Troe parameters: $a = 0.7507$, $T^* = 1302.0$, $T^{**} = 4167.0$, $T^{***} = 98.5$				
	Enhanced third-body efficiencies: $H_2 = 2.0$, $Ar = 0.70$				
22.[a]	$C_2H_3 + H (+M) \Leftrightarrow C_2H_4 (+M)$				[25]
	High-pressure limit:	6.08×10^{12}	0.27	280	
	Low-pressure limit:	1.40×10^{30}	-3.86	3320	
	Troe parameters: $a = 0.7820$, $T^* = 2663.0$, $T^{**} = 6095.0$, $T^{***} = 207.5$				
	Enhanced third-body efficiencies: $H_2 = 2.0$, $CH_4 = 2.0$, $C_2H_6 = 3.0$, $Ar = 0.70$				
23.[a]	$C_2H_4 + H(+M) \Leftrightarrow C_2H_5(+M)$				[25]
	High-pressure limit:	1.08×10^{12}	0.454	1820	
	Low-pressure limit:	1.20×10^{42}	-7.62	6970	
	Troe parameters: $a = 0.9753$, $T^* = 984.0$, $T^{**} = 4374.0$, $T^{***} = 210.0$				
	Enhanced third-body efficiencies: $H_2 = 2.0$, $Ar = 0.70$				
24.[a]	$C_2H5 + H(+M) \Leftrightarrow C_2H_6(+M)$				[25]
	High-pressure limit:	5.21×10^{17}	-0.99	1580	
	Low-pressure limit:	1.99×10^{41}	-7.08	6685	
	Troe parameters: $a = 0.8422$, $T^* = 2219.0$, $T^{**} = 6882.0$, $T^{***} = 125.0$				
	Enhanced third-body efficiencies: $H_2 = 2.0$, $Ar = 0.70$				
C$_1$H$_x$–C$_2$H$_y$ coupling reactions					
25.	$C_2 + M \Leftrightarrow 2C + M$	1.50×10^{16}	0	142 400	[29]
26.[a]	$C + CH \Leftrightarrow C_2 + H$	2.00×10^{14}	0	0	[31]
27.[a]	$C + CH_2 \Leftrightarrow C_2H + H$	5.00×10^{13}	0	0	[25]
28.[a]	$C + CH_3 \Leftrightarrow C_2H_2 + H$	5.00×10^{13}	0	0	[25]
29.	$2CH \Leftrightarrow C_2H + H$	1.50×10^{14}	0	0	[31]
30.	$CH + CH_2 \Leftrightarrow C_2H_2 + H$	4.00×10^{13}	0	0	[25]
31.	$CH + CH_3 \Leftrightarrow C_2H_3 + H$	3.00×10^{13}	0	0	[25]
32.	$CH + CH_4 \Leftrightarrow C_2H_4 + H$	9.24×10^{15}	-0.9	0	[33]
33.	$2CH_2 \Leftrightarrow C_2H_2 + H_2$	1.60×10^{15}	0	12 000	[32]
34.	$2CH_2 \Leftrightarrow C_2H_2 + 2H$	2.00×10^{14}	0	11 000	[32]
35.[a]	$CH_2 + CH_3 \Leftrightarrow C_2H_4 + H$	3.00×10^{14}	0	0	[25]

Table 2 (continued)
Gas-phase reaction mechanism. Forward rate constants are expressed in the form $k_f = AT^\beta exp(-E/RT)$

Reaction		A (cm^3 mol s)	β	E_a (cal/mol)	Reference
36.[a]	$2CH_3 \Leftrightarrow C_2H_5 + H$	5.00×10^{12}	0.1	10 600	[25]
37.[a]	$2CH_3(+M) \Leftrightarrow C_2H_6(+M)$				[25]
	High-pressure limit:	2.12×10^{16}	-0.97	622	
	Low-pressure limit:	1.77×10^{50}	-9.67	6220	
	Troe parameters: $a = 0.5325$, $T^* = 1038.0$, $T^{**} = 4970.0$, $T^{***} = 151.0$				
	Enhanced third-body efficiencies: $H_2 = 2.0$, Ar $= 0.70$				
Singlet methylene reactions					
38.[a]	$CH_2(S) + Ar \Leftrightarrow CH_2 + Ar$	9.00×10^{12}	0	600	[25]
39.	$CH_2(S) + H \Leftrightarrow CH + H_2$	3.00×10^{13}	0	0	[25]
40.[a]	$CH_2(S) + H_2 \Leftrightarrow CH_3 + H$	7.00×10^{13}	0	0	[25]
41.[d]	$CH_2(S) + C \Leftrightarrow C_2H + H$	5.00×10^{13}	0	0	
42.[e]	$CH_2(S) + CH \Leftrightarrow C_2H_2 + H$	4.00×10^{12}	0	-570	
43.[d]	$CH_2(S) + CH_2 \Leftrightarrow C_2H_3 + H$	8.00×10^{12}	0	-570	
44.[d]	$2CH_2(S) \Leftrightarrow C_2H_3 + H$	8.00×10^{12}	0	-570	
45.	$CH_2(S) + CH_3 \Leftrightarrow C_2H_4 + H$	1.20×10^{13}	0	-570	
46.	$CH_2(S) + CH_4 \Leftrightarrow 2CH_3$	1.60×10^{13}	0	-570	[25]

[a] Included in the reduced mechanism for thc two-dimensional boundary layer model.
[b] Compromise between Refs. [34,35]. Written in reverse direction and factor of two smaller than measurement by [36].
[c] Falloff reactions in the Troe form [34].
[d] Same as reaction 27.
[e] Estimate, based on Ref. [25] values for $CH_2(S) + CH_4$ and $CH_2(S) + CH_3$.

previously been neglected due to a calculation error [38], but the pressure dependence for this reaction is significant at 4000 K and 1 atm.

The two-dimensional boundary layer model uses a subset of the full reaction mechanism obtained by using a mechanism reduction based on principle component analysis. This substantially reduced the computational expense of the two-dimensional modeling with minimal effect on the results. The reduced reaction set is noted in Table 2.

The boundary conditions for species mole fractions at the edge of the boundary layer are based on an equilibrium calculation. At 4000 K and 1 atm chemical equilibrium is a reasonable assumption. An iterative scheme determines the freestream elemental inputs of argon, hydrogen and carbon necessary for the equilibrium calculation. Iteration is necessary for two reasons. The GC measurements for typical conditions indicated that the gas composition on the flow axis was hydrogen-enriched by a factor of about 3.0, and carbon-enriched by a factor of about 4.5, relative to complete mixing. Incomplete mixing can be explained by the high velocity of the reactant jet (~ 100 m/s at the injector exit compared with ~ 10 m/s for the surrounding argon), and uneven mixing can be explained by the higher diffusivity of hydrogen compared with hydrocarbons.

The iterative procedure begins by estimating the elemental fractions at the boundary layer edge using the GC measurements. An equilibrium calculation is performed to determine the mixture composition at that location, and the boundary layer model is executed. The elemental fractions predicted at the exit of the sampling orifice are then compared with the GC measurements. If they disagree, the freestream elemental fractions are adjusted, and the process is repeated until the predicted elemental fractions exiting the sampling orifice match the GC measurements.

A one-dimensional model of the gas sampling line is used to simulate changes in chemical composition as the gas travels from the sampling orifice to the gas chromatograph. Two factors reduce the sampling line chemistry to essentially only reactions involving hydrocarbon radicals: (1) atomic hydrogen is rapidly destroyed by reactions on the sampling line walls [14], and (2) reactions with stable molecules have significant activation barriers and proceed slowly under the conditions of the sampling line (10–20 Torr, 300 K). However, hydrocarbon radical recombination has a significant effect on the chemical composition, so kinetic modeling is necessary to determine which stable species are produced by this process.

The computational domain of the sampling line model extends from approximately 2 mm downstream of the sampling orifice, through a 60 cm long stainless steel tube that extends to the gas chromatograph. Because the predicted mole fractions of all reactive radicals are less than 1 ppm after 20 cm, the computational domain is truncated at 20 cm. The chemistry in the sampling line was modeled using PREMIX, a program for modeling steady laminar one-dimensional premixed flames [39]. This is equivalent to a one-dimensional model of a plug-flow tubular reactor with axial mixing by molecular diffusion. The mixture composition at the inlet of the sampling line model is taken from the sampling orifice outlet composition predicted

by the boundary layer calculation, with one exception. The atomic hydrogen mole fraction is set to approximately zero (1×10^{-20}), and the molecular hydrogen mole fraction is increased by the corresponding amount. This simulates rapid recombination of hydrogen on the walls of the sampling line, which can be shown to be four orders of magnitude faster than homogeneous recombination for the conditions of the sampling line [40]. A zero concentration gradient boundary condition is imposed at the sampling line outlet. Surface reactions on the tube walls are neglected for all species other than atomic hydrogen. The gas temperature is assumed to equal the sampling line wall temperature and a simple one-dimensional heat transfer model determines the wall temperature.

4. Results and discussion

A complete description and discussion of the two-dimensional boundary layer model is presented elsewhere [5]. It was found that gas sampling distorts the temperature and velocity profiles significantly, raising the gas temperature and velocity in the orifice relative to their values at the surface in the absence of the orifice. This can cause significant differences between the sampled gas composition and the gas composition at the surface away from the sampling orifice, which is essentially identical to the composition that would exist at the location of the orifice if the orifice were not present. As an example, the predicted effect of the

sampling disturbance on the methane mole fraction is shown in Fig. 2, which was calculated for an input methane/hydrogen ratio of 2% and a substrate temperature of 1200 K. The composition distortion is significant for those species formed or destroyed in a chemical boundary layer whose thickness is comparable to the dimensions of the sampling disturbance (~ 100 μm) [5].

Fig. 3 shows predicted species profiles across the boundary layer at a radial location 2 mm from the sampling orifice, for the same conditions. Because methane, ethylene and ethane have relatively steep mole fraction gradients near the surface, their sampled concentrations at the orifice outlet are smaller by factors of approximately two, three, and six respectively, compared with their mole fractions at the surface at a radial location 2 mm from the sampling orifice. Accounting for the sampling disturbance improved the agreement between the model predictions and the measured concentrations, relative to our preliminary modeling results [4].

Fig. 4 shows the temperature profile and predicted composition changes that occur in the first 10 cm of the gas sampling line for a sampling line pressure of 20 Torr. The sampling line temperature drops from the substrate temperature to the temperature of the cooling water within the first centimeter. The different slopes of the temperature profile are due to materials with different thermal conductivities that compose the substrate assembly in this region (molybdenum, Inconel and copper).

In Fig. 4 it is seen that carbon, methyl and methylene radicals are all predicted to be destroyed by homogeneous recombination in the sampling line, forming the
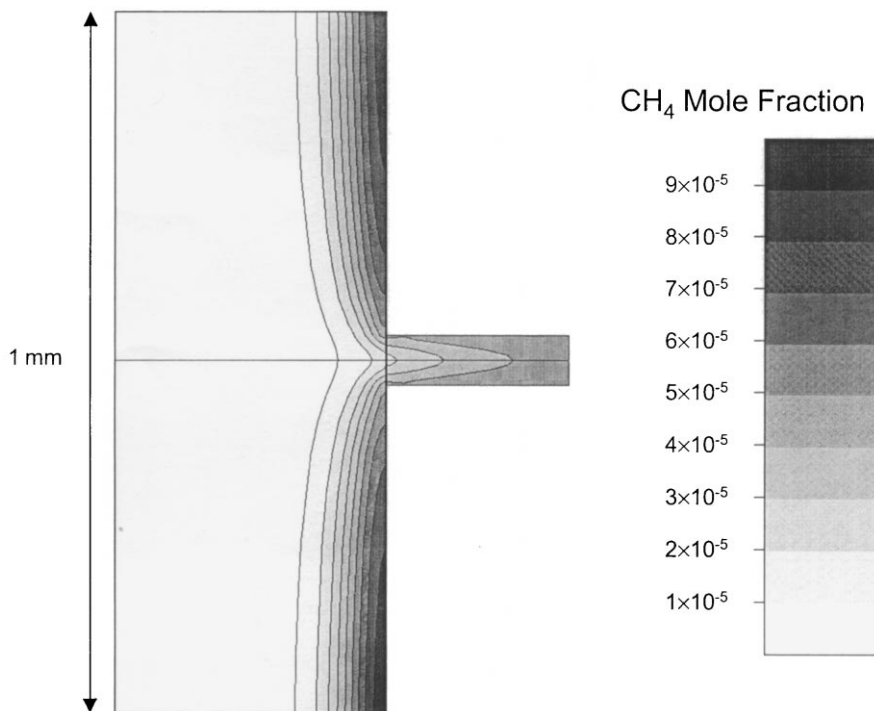

Fig. 2. Predicted effect of the sampling disturbance on the methane mole fraction.
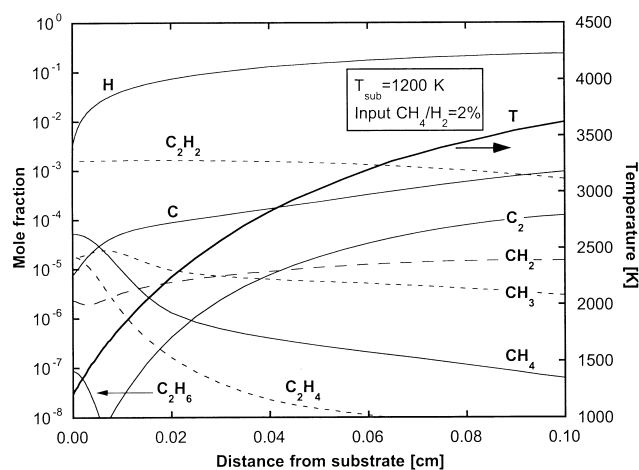
Fig. 3. Predicted species profiles across the boundary layer at a radial location 2 mm from the sampling orifice.

stable hydrocarbons methane, ethylene and ethane. In the work by Harris and Weiner [14] the 'radical scavenging' approach was used. This approach is applicable when radicals recombine to form stable species that are otherwise not present in the sampling system. It was found by Harris and Weiner [14] that C_2H_4 and C_2H_6 were formed by methyl recombination in their sampling line, and their model predicted negligible concentrations of C_2H_4 and C_2H_6 at the substrate surface. As a result, the mole fraction of methyl at the surface in their work was simply estimated to equal twice the sum of C_2H_4 and C_2H_6 detected by GC. However, because the mole fractions of C_2H_4, C, CH_2, and CH_3 at the sampling line inlet for our system are not negligible — these four species are all predicted to have greater than 1 ppm mole fractions, and they sum to almost 100 ppm — it is not possible in our case to use the simple approach of Harris and Weiner [14] to estimate the inlet methyl
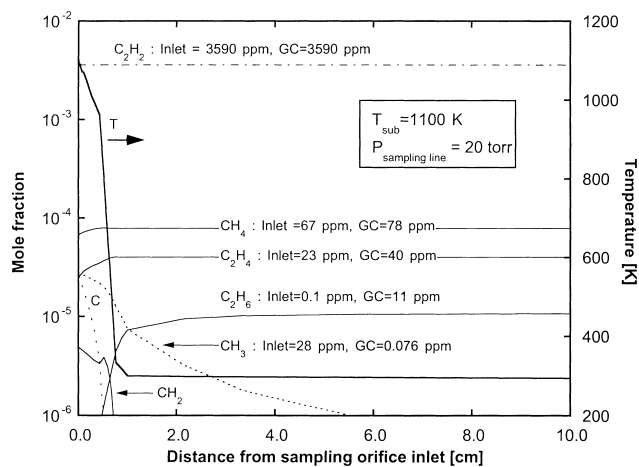
concentration. Consequently, the more detailed treatment presented here is necessary.

Figs. 5 and 6 show a comparison of model predictions with GC measurements for CH_4, C_2H_2, C_2H_4 and C_2H_6 mole fractions as substrate temperature and input methane/hydrogen ratio are varied. The model predictions shown are the mole fractions at the downstream end of the sampling line model, which correspond to the mole fractions arriving at the gas chromatograph. The CH_4, C_2H_2, and C_2H_4 mole fraction measurements shown in Figs. 5 and 6 are from measurements made approximately 30 min after the start of the diamond growth experiments, which was long enough to ensure that a continuous diamond film had formed on the molybdenum substrates, but short enough to avoid clogging of the orifice by diamond growth. Because C_2H_6 was at mole fractions near the detection limit of the flame ionization detector (~ 10 ppm), it was only

Fig. 4. Temperature profile and predicted composition changes in the first 10 cm of the gas sampling line; line pressure 20 Torr.
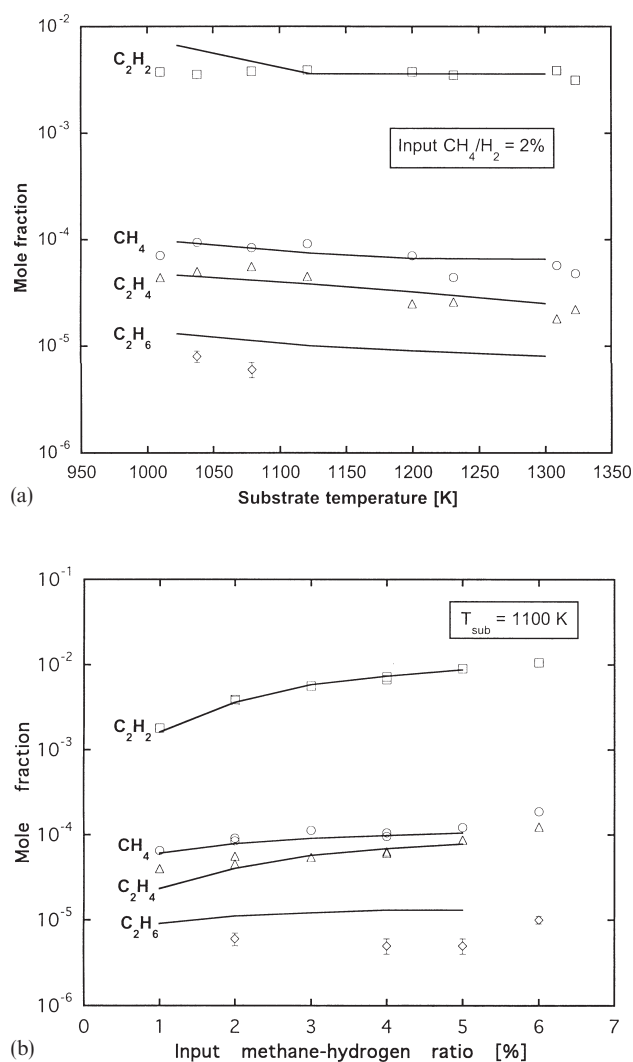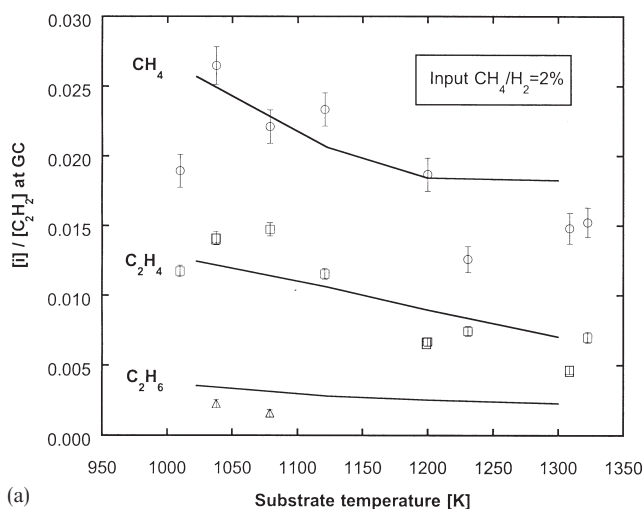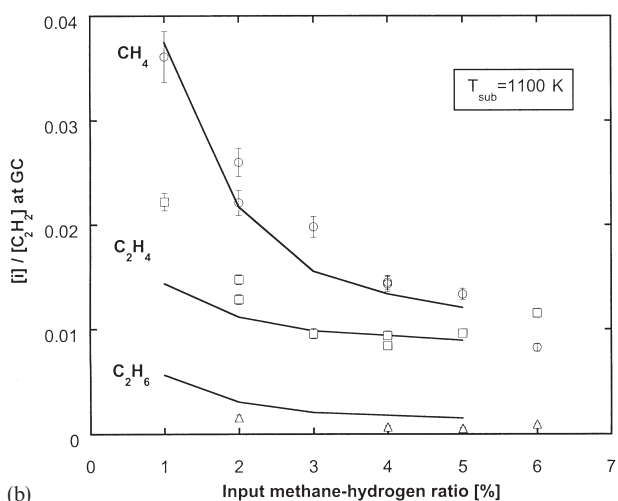
Fig. 5. Predicted mole fractions of CH_4, C_2H_2, C_2H_4 and C_2H_6 (lines) compared with GC measurements (symbols): (a) versus substrate temperature; (b) versus input methane/hydrogen ratio at 1100 K.

(a)

(b)

Fig. 6. Mole fractions of CH_4, C_2H_4 and C_2H_6 normalized by the mole fraction of C_2H_2: predicted (lines) compared with GC measurements (symbols). Variation with: (a) substrate temperature; (b) input methane/hydrogen ratio at 1100 K.

occasionally measured. The measurements of C_2H_6 shown are for the times closest to 30 min after the start of the experiment, for those cases where one or more measurements were available.

In Fig. 5a and b the predicted mole fractions of CH_4, C_2H_2, C_2H_4 and C_2H_6 are compared with GC measurements, and in Fig. 6a and b the mole fractions have been normalized by the mole fraction of C_2H_2 and plotted on a linear scale to make trends more evident. As seen in Fig. 5, the model predictions are in accord with the experimental observation that over 90% of the carbon reaching the gas chromatograph is in the form of acetylene for all conditions studied.

Increasing the substrate temperature at a fixed input methane/hydrogen ratio of 2% causes the concentration ratios at the gas chromatograph of CH_4, C_2H_4 and C_2H_6 to C_2H_2 to all decrease, as seen in Fig. 6a. The

methane/acetylene ratio decreases as the substrate temperature increases from 1000 to 1200 K and then levels off. The ethylene/acetylene ratio decreases over the entire temperature range shown, dropping by a factor of about two over the temperature range from 1000 to 1350 K. The ethane/acetylene ratio decreases modestly with increasing substrate temperature. The agreement between the model predictions and the experimental measurements is quite satisfactory, in regard both to these qualitative trends and to the absolute magnitude of these concentration ratios.

Fig. 6b shows the effect on these same concentration ratios of varying the input methane/hydrogen ratio from 1 to 6% at a fixed substrate temperature of 1100 K. All of these concentration ratios decrease with increasing input methane/hydrogen ratio. Again there is generally good agreement between the model predictions and the GC measurements.

Although the good agreement between the GC measurements and the predicted gas composition at the gas chromatograph does not unambiguously prove that the model accurately predicts gas composition, including radical species, at the diamond growth surface, it does at least provide evidence in support of the model's validity. It is, therefore, of interest to use the model to explore how changes in substrate temperature and input methane/hydrogen ratio affect the predicted gas composition at the diamond surface. The gas composition at the growth surface was predicted using the SPIN code, from the CHEMKIN package which models one-dimensional reacting stagnation-point flow problems [41]. Whereas the two-dimensional model utilizes a reduced reaction set, the full gas-phase and surface reaction mechanisms were used for these calculations. Because the sampling disturbance does not affect the flow at points radially distant from the orifice, the one-dimensional treatment is expected to be accurate in this region. Fig. 7 shows the atomic hydrogen boundary layer profiles calculated by the one-dimensional model, and by the two-dimensional model at a location 2 mm radially distant from the sampling orifice. For atomic hydrogen (Fig. 7) and all of the other species, the two-dimensional and one-dimensional calculations are nearly identical. Also, the one-dimensional model is capable of adaptively refining the computational grid near the substrate surface, so it is expected to be more accurate in the near-surface region where several species have steep concentration gradients (Fig. 3).

Fig. 8a and b show how the predicted concentration ratios of atomic hydrogen, methyl and acetylene change as substrate temperature and input methane-hydrogen ratio are varied. Absolute values of the concentrations of atomic hydrogen, methyl, acetylene and atomic carbon are shown in Table 3. These results suggest that, in addition to methyl, acetylene and atomic carbon may be important growth species during atmospheric-pres-
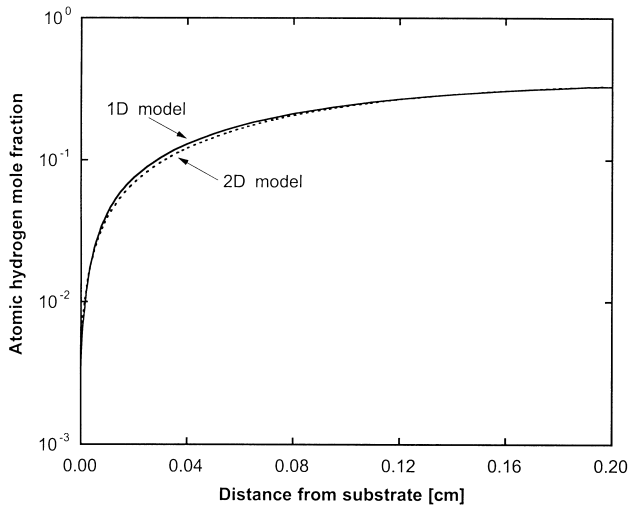
Fig. 7. Atomic hydrogen boundary layer profiles calculated by the one-dimensional model, and by the two-dimensional model at a location 2 mm radially distant from the sampling orifice.

sure RF plasma diamond CVD. Experimental studies [42] have indicated that the sticking coefficient of acetylene on the diamond growth surface is roughly two orders of magnitude below that of methyl. However, Fig. 8a and b show that the predicted concentration of acetylene at the growth surface is 100 to 200 times higher than that of methyl. In addition, recent kinetic Monte Carlo simulations show that C_2H_2 may significantly affect diamond film morphology [43]. It thus appears likely that C_2H_2 plays an important role in diamond growth in this relatively acetylene-rich environment.

As seen in Table 3, for an input methane/hydrogen ratio of 2%, the predicted concentration ratio of C to CH_3 at the growth surface ranges from 18 to 52% as the substrate temperature varies from 1023 to 1300 K. It is reasonable to assume that the reactivity of C atoms at the diamond growth surface is at least as high or somewhat higher than that of methyl radicals. In the extended growth-by-methyl mechanism [18], the reactivity of C at the surface is assumed to be twice that of CH_3. Thus, as has been previously noted [8,18], atomic
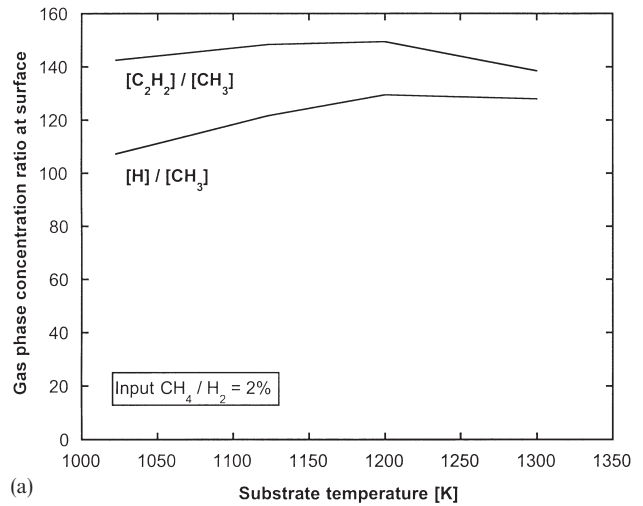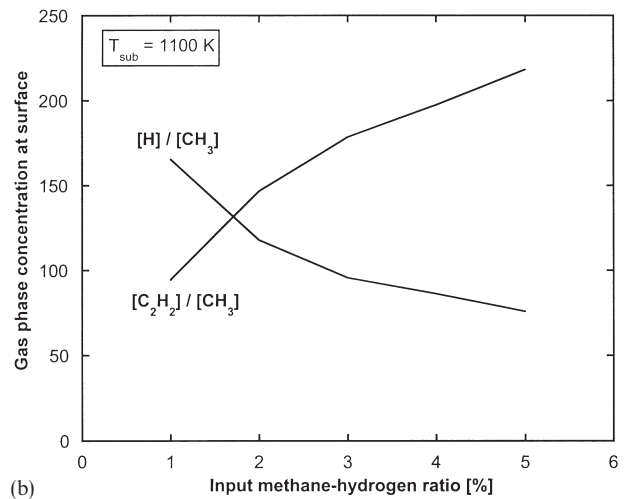
Fig. 8. Change in predicted concentration ratios of atomic hydrogen, methyl and acetylene as a function of (a) substrate temperature and (b) input methane/hydrogen ratio at 1100 K.

carbon may be an important growth species in thermal plasma diamond CVD, and its importance is expected to become even more pronounced for flow configurations such as DC arc jets and accelerated RF plasmas,

Table 3
Surface concentrations of hydrogen, methyl, acetylene, and atomic carbon

| Substrate temperature (K)	Input CH_4/H_2 ratio (%)	[H] (cm^{-3})	[CH_3] (cm^{-3})	[C_2H_2] (cm^{-3})	[C] (cm^{-3})
1023	2	1.7×10^{16}	1.6×10^{14}	2.2×10^{16}	2.9×10^{13}
1123	2	1.7×10^{16}	1.4×10^{14}	2.0×10^{16}	4.6×10^{13}
1200	2	1.7×10^{16}	1.3×10^{14}	2.0×10^{16}	5.5×10^{13}
1300	2	1.7×10^{16}	1.1×10^{14}	1.8×10^{16}	5.7×10^{13}
1100	1	1.7×10^{16}	1.0×10^{14}	9.3×10^{15}	3.3×10^{13}
1100	2	1.7×10^{16}	1.4×10^{14}	2.1×10^{16}	4.0×10^{13}
1100	3	1.7×10^{16}	1.7×10^{14}	3.1×10^{16}	4.7×10^{13}
1100	4	1.7×10^{16}	2.0×10^{14}	3.9×10^{16}	4.7×10^{13}
1100	5	1.7×10^{16}	2.3×10^{14}	4.9×10^{16}	5.3×10^{13}
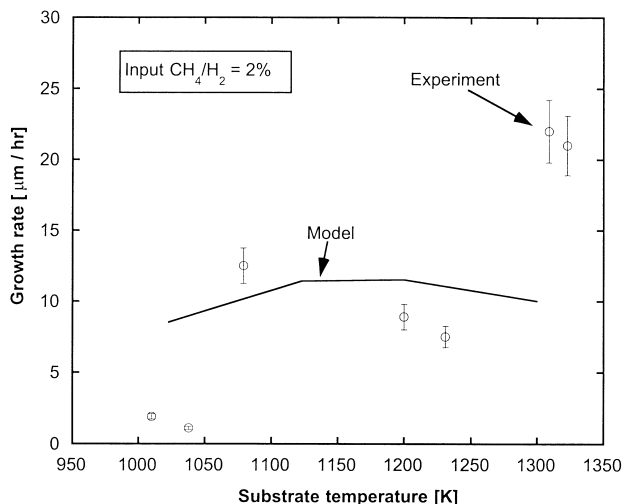
Fig. 9. Comparison of the model predictions for film growth rate with the measured average linear growth rate as a function of substrate temperature.

which produce higher velocities and thinner boundary layers [18].

Fig. 9 compares the model predictions for film growth rate with the measured average linear growth rate as the substrate temperature was varied. For an input CH_4/H_2 ratio of 2%, the experimental growth rates varied from 1 to 20 μm/h as the substrate temperature was increased from 1000 to 1300 K. All of these cases produced continuous, well-faceted diamond films, which were grown for at least 4 h. The experimental growth rates were determined by measuring the film thickness after the experiment. Growth rate uncertainty was estimated to be $\pm 10\%$.

The extended growth-by-methyl mechanism [18] performs well for moderate temperatures (~ 1100 to 1230 K). However, at low temperature (~ 1000 K) it overpredicts growth rate by an order of magnitude, whereas at high temperature (~ 1300 K) it underpredicts the growth rate by about a factor of two. Two diamond

growth experiments were made at both the low and high temperature extremes, and the growth rates were shown to be repeatable. Referring to Fig. 8a and to Table 3, there are no changes in absolute or relative gas-phase species concentrations at the growth surface that could account for the order of magnitude change in growth rate. In fact, the near-surface concentrations of the potential growth species methyl and acetylene decrease as the substrate temperature increases, while the concentration of C doubles over this range and the H-atom concentration is flat. Although this does not provide sufficient evidence to draw firm conclusions, it suggests that the discrepancy is due to temperature-dependent surface kinetics not correctly modeled in the growth mechanism. This is not surprising, as the previous work on which our surface mechanism is based [18,20,21] was all developed specifically for conditions at 1200 K. A number of studies, reviewed in Ref. [18] have indicated that this mechanism predicts experimental growth rates within a factor of two for a variety of diamond growth environments with the substrate temperature close to 1200 K, but to our knowledge these mechanisms have not previously been extended to higher or lower temperatures, although they do include estimated activation energies for all of the reactions involving abstraction of surface hydrogen atoms. We implemented temperature dependence by utilizing these activation energies, and by estimating thermochemical properties assuming constant specific heat for each of the surface species in the mechanism. These specific heats were estimated using enthalpies and entropies at 1200 K calculated in molecular mechanics simulations by Harris and Goodwin [21]. Although our mechanism, as with previous studies, predicts the growth rate well for substrate temperatures near 1200 K, our attempt to extend the mechanism obviously fails at the low- and high-temperature ends. It should be reiterated that our growth mechanism includes only C_1 radicals as growth species, and thus does not include acetylene, which is exceptionally abun-

Table 4
Comparison of surface species concentrations for four different diamond CVD systems

CVD system	[H] (cm^{-3})	[CH$_3$] (cm^{-3})	[C$_2$H$_2$] (cm^{-3})	[H]/[CH$_3$]	[C$_2$H$_2$]/[CH$_3$]	Pressure (Torr)	Substrate temperature (K)
Hot filament[a] [16]	3.7×10^{14}	6.7×10^{13}	7.4×10^{14}	5.5	11	20	1200
Hot filament[b] [44]	1.1×10^{15}	1.3×10^{14}	1.8×10^{14}	8.5	1.4	23	1200
Microwave[c] [45]	1.1×10^{14}	2.7×10^{13}	2.3×10^{14}	4.1	8.5	20	1200
Low pressure flame[d] [11]	7.5×10^{15}	5.7×10^{14}	5.6×10^{16}	13.2	98	35	900
Low pressure flame[e] [12]	1.2×10^{15}	2.3×10^{14}	5.8×10^{15}	5.2	25	47	1013
RF thermal plasma (this work)	1.7×10^{16}	1.3×10^{14}	1.9×10^{16}	131	146	760	1200

[a] Concentrations are taken from mass spectrometer measurements.
[b] Concentrations are taken from REMPI and mass spectrometer measurements.
[c] Concentrations are taken from mass spectrometer measurements.
[d] Concentrations are taken from a model validated by LIF and mass spectrometer measurements of CH$_4$, C$_2$H$_2$, OH, CO, and H$_2$.
[e] Concentrations are taken from a model validated by mass sprectrometer measurements of CO, CO$_2$, H$_2$, Ar, CH$_4$, C$_2$H$_2$, and H$_2$O.

dant under our conditions. Furthermore, phenomena such as etching, surface diffusion, and growth of non-diamond carbon are neglected. In short, our results indicate that our surface mechanism is too simplistic to capture temperature effects.

Finally, Table 4 shows a comparison of H, CH_3 and C_2H_2 near-surface species concentrations for four different diamond CVD environments: hot filament, microwave, low-pressure flame and RF thermal plasma. The data shown in Table 4 are from either direct experimental measurements [16,44,45] or from the predictions of experimentally validated models [11,12]. The measurements or model predictions shown were all taken at a substrate temperature of 1200 K if such data were available; otherwise the data shown are for the reported substrate temperature closest to 1200 K. The results can be grouped into three categories: (1) low-pressure diffusion-dominated systems (hot filament and microwave); (2) low-pressure convection-dominated systems (flame) and (3) atmospheric-pressure convection-dominated systems (RF thermal plasma). Differences within each of these categories may be attributed to different configurations and operating conditions.

Table 4 shows that there are substantial differences between atmospheric-pressure RF thermal plasma and the other diamond CVD environments. For the RF thermal plasma, the H/CH_3 ratio is 10 to 30 times greater than in any of the other systems. Also, the C_2H_2/CH_3 ratio is 10 to 100 times greater than in the hot filament or microwave systems, and from 1.5 to 5 times higher than in the flame systems. Clearly, the chemical environments at the diamond growth surface for hot filament, microwave, flame and RF thermal plasma diamond CVD systems are significantly different.

5. Summary and conclusions

Detailed numerical simulations were compared with gas chromatograph measurements of the chemical composition of gas sampled through a small orifice located in the center of the growth substrate during atmospheric-pressure RF plasma diamond CVD. The numerical model included a two-dimensional analysis of the sampling disturbance in the thin boundary layer above the substrate, accounted for chemistry in the gas chromatograph sampling line, and utilized a reaction mechanism that was significantly revised from a previously reported version. Predictions of CH_4, C_2H_2, C_2H_4 and C_2H_6 concentrations reaching the gas chromatograph agreed well with the measurements of those species. Predicted diamond growth rates were in good agreement with measurements at moderate substrate temperature, but the agreement was poor at low ($\sim$1000 K) and high ($\sim$1300 K) substrate temperatures. We attribute this discrepancy to temperature-dependent changes in the surface reaction kinetics, not correctly accounted for in the model. Previously reported measurements and modeling predictions of surface chemistry for three other diamond CVD environments (hot filament, microwave and low-pressure flame) were compared with the present results. It was found that the chemical environment at the growth surface for an atmospheric-pressure RF thermal plasma differs significantly from the other three systems, having substantially higher H/CH_3 and C_2H_2/CH_3 concentration ratios near the growth surface. The concentration ratio of acetylene to methyl at the growth surface was predicted to equal approximately 150 for typical operating conditions. Based on studies in the literature of the relative reactivities of methyl and acetylene at the diamond surface, this suggests that acetylene may play a significant role during thermal plasma diamond CVD.

References

[1] T.G. Owano, C.H. Kruger, D.S. Green, S. Williams, R.N. Zare, Diamond Relat. Mater. 2 (1993) 661.
[2] T.G. Owano, E.H. Wahl, C.H. Kruger, Proceedings of the 8th CIMTEC-World Ceramics Conference and Forum on New Materials, Florence, Italy, (1994).
[3] J.W. Lindsay, J.M. Larson, S.L. Girshick, Diamond Relat. Mater. 6 (1997) 481.
[4] S.L. Girshick, J.M. Larson, Pure Appl. Chem. 70 (1998) 485.
[5] M.T. Swihart, S.L. Girshick, Phys. Fluids 11 (1999) 821.
[6] J.A. Miller, C.F. Melius, Combust. Flame 91 (1992) 21.
[7] S.J. Harris, J. Appl. Phys. 65 (1989) 3044.
[8] M.E. Coltrin, D.S. Dandy, J. Appl. Phys. 74 (1993) 5803.
[9] M. Frenklach, H. Wang, Phys. Rev. B 43 (1991) 1520.
[10] S.L. Girshick, C. Li, B.W. Yu, H. Han, Plasma Chem. Plasma Process. 13 (1993) 169.
[11] N.G. Glumac, D.G. Goodwin, Combust. Flame 105 (1996) 321.
[12] C.A. Wolden, R.F. Davis, Z. Sitar, J.T. Prater, J. Mater. Res. 12 (1997) 2733.
[13] S.J. Harris, D.N. Belton, A.M. Weiner, S.J. Schmieg, J. Appl. Phys. 66 (1989) 5353.
[14] S.J. Harris, A.M. Weiner, J. Appl. Phys. 67 (1990) 6520.
[15] D.G. Goodwin, G.G. Gavillet, J. Appl. Phys. 68 (1990) 6393.
[16] M.C. McMaster, W.L. Hsu, M.E. Coltrin, D.S. Dandy, J. Appl. Phys. 76 (1994) 7567.
[17] S.L. Girshick, B.W. Yu, C. Li, H. Han, Diamond Relat. Mater. 2 (1993) 1090.
[18] B.W. Yu, S.L. Girshick, J. Appl. Phys. 75 (1994) 3914.
[19] M.T. Bieberich, S.L. Girshick, Plasma Chem. Plasma Process. 16 (1996) 157S.
[20] S.J. Harris, Appl. Phys. Lett. 56 (1990) 2298.
[21] S.J. Harris, D.G. Goodwin, J. Phys. Chem. 97 (1993) 23.

[22] CFD-ACE Command Language Reference Manual, Version 2.1, Report CFDRC GR-97-30, CFD Research Corp., Huntsville, AL, 1997.

[23] J.O. Hirschfelder, C.F. Curtiss, R.B. Bird, Molecular Theory of Gases and Liquids, Wiley, New York, 1954.

[24] R.J. Kee, G. Dixon-Lewis, J. Warnatz, M.E. Coltrin, J.A. Miller, Report SAND87-8215B, Sandia National Laboratories, 1986.

[25] C.T. Bowman, R.K. Hanson, W.C. Gardiner, V. Lissianski, M. Frenklach, M. Goldenberg, G.P. Smith, GRI-Mech homepage (1999)

[26] A.J. Dean, D.F. Davidson, R.K. Hanson, J. Phys. Chem. 95 (1991) 183.

[27] S. Zabarhick, J.W. Fleming, M.C. Lin, J. Chem. Phys. 85 (1986) 4373.

[28] V.D. Knyazev, A. Bencsura, S.I. Stoliarov, I.R. Slagle, J. Phys. Chem. 100 (1996) 11 346.

[29] T. Kruse, P. Roth, J. Phys. Chem. 101 (1997) 2138.

[30] J. Peeters, H. Van Look, B. Ceursters, J. Phys. Chem. 100 (1996) 15 124.

[31] A.J. Dean, R.K. Hanson, Int. J. Chem. Kinet. 24 (1992) 517.

[32] S. Bauerle, M. Klatt, H.G. Wagner, Ber. Bunsenges. Phys. Chem. 99 (1995) 870.

[33] M.A. Blitz, D.G. Johnson, M. Pesa, M.J. Pilling, S.H. Robertson, P.W. Seakins, J. Chem. Soc. Faraday Trans. 93 (1997) 1473.

[34] R.G. Gilbert, K. Luther, J. Troe, Ber. Bunsenges. Phys. Chem. 87 (1983) 169.

[35] D.L. Baulch, C.J. Cobos, R.A. Cox, C. Esser, P. Frank, T. Just, J.A. Kerr, M.J. Pilling, J. Troe, R.W. Walker, J. Warnatz, J. Phys. Chem. Ref. Data 21 (1992) 411.

[36] P.S. Monks, F.L. Nesbitt, W.A. Payne, M. Scanlon, L.J. Stief, J. Phys. Chem. 99 (1995) 17 151.

[37] R.J. Kee, F.M. Rupley, J.A. Miller, Report SAND87-8215B, Sandia National Laboratories, 1990.

[38] B.W. Yu, Ph.D. dissertation, University of Minnesota, 1994.

[39] R.J. Kee, J.F. Crcar, M.D. Smooke, J.A. Miller, Report SAND85-8240, Sandia National Laboratories, 1985.

[40] J.W. Lindsay, Ph.D. dissertation, University of Minnesota, 1998.

[41] M.E. Coltrin, R.J. Kee, G.H. Evans, E. Meeks, F.M. Rupley, J.F. Grcar, Report SAND91-8003, Sandia National Laboratories, 1991.

[42] M.H. Loh, M.A. Cappelli, Appl. Phys. Lett. 70 (1997) 1052.

[43] C.C. Battaile, D.J. Srolovitz, J.E. Butler, Diamond Relat. Mater. 6 (1997) 1198.

[44] V. Zumbach, J. Schafer, J. Tobai, M. Ridder, T. Dreier, T. Schaich, J. Wolfrum, B. Ruf, F. Behrendt, O. Deutschman, J. Warnatz, J. Chem. Phys. 107 (1997) 5918.

[45] M.C. McMaster, W.L. Hsu, M.E. Coltrin, D.S. Dandy, C. Fox, Diamond Relat. Mater. 4 (1995) 1000.